Considering the Higher-Order Effect of Residual Modes in the Craig–Bampton Method

Jaemin Kim,* Seung-Hwan Boo,† and Phill-Seung Lee‡
Korea Advanced Institute of Science and Technology, Daejeon 34141, Republic of Korea

DOI: 10.2514/1.J055666

In this paper, the accuracy of the Craig–Bampton method, one of the most widely used component mode synthesis methods, is improved. Considering the higher-order effect of residual modes that are simply truncated in the Craig–Bampton method, the original finite element model can be more accurately reduced. In this formulation, unknown eigenvalues are considered as additional generalized coordinates, which can be eliminated by employing the concept of system equivalent reduction expansion process. The new component mode synthesis is named the higher-order Craig–Bampton method. The formulation of the higher-order Craig–Bampton method is presented, and its improved accuracy is demonstrated through various examples.

Nomenclature

$\boldsymbol{F}$	=	residual flexibility matrix
$\boldsymbol{K}$	=	stiffness matrix
$\boldsymbol{M}$	=	mass matrix
$\boldsymbol{q}$	=	modal coordinate vector
$\boldsymbol{T}$	=	transformation matrix
$\boldsymbol{u}$	=	displacement vector
$\boldsymbol{\Lambda}$	=	eigenvalue matrix
λ	=	eigenvalue
Φ	=	eigenvector matrix
$\boldsymbol{\varphi}$	=	eigenvector
$\boldsymbol{\Psi}$	=	constraint mode matrix

I. Introduction

COMPONENT mode synthesis (CMS) methods have been widely used in finite element (FE) analysis of structural dynamics problems. CMS methods are very effective for calculating modal solutions (mode shapes and natural frequencies) of complicated and large FE models, which usually consist of many substructures [1–25]. CMS methods have also been frequently employed to reduce the number of degrees of freedom (DOFs) of structural dynamics models for airplane, automobile, and ship structures [1,2].

After Hurty's pioneering work in 1965 [3], various CMS methods have been developed; see [4–25]. The methods have different characteristics and advantages. Among them, the Craig–Bampton method has been mostly widely used due to its simplicity and robustness. In the Craig–Bampton (CB) method [4], a structural FE model is represented by an assemblage of substructures that are connected through a fixed interface boundary. The modal solution of the original FE model is synthesized by selecting only dominant modes obtained solving the substructural eigenvalue problems, and the remaining modes not selected are designated as the residual modes. To define the dominant and residual modes appropriately, several mode selection methods [5–7] have been well studied.

Received 8 September 2016; revision received 18 July 2017; accepted for publication 13 August 2017; published online 19 September 2017.

*Graduate Student, Graduate School of Ocean Systems Engineering; oceaneng@kaist.ac.kr. Student Member AIAA.

†Postdoctoral Researcher, Department of Mechanical Engineering; shboo@kaist.ac.kr. Member AIAA.

‡Associate Professor, Department of Mechanical Engineering; phillseung@kaist.edu. Member AIAA.

Recently, considering the first-order effect of the residual modes, the CB method was significantly improved by Kim and Lee [19]. The new method is named the enhanced CB method (ECB), in which the unknown eigenvalue included in the formulation is replaced with the multiplication of the inverse matrix of the reduced mass matrix and the reduced stiffness matrix, which are the already-known matrices, by adopting O'Callahan's idea [26]. Then, there is a natural question: what happens if the second-, third-, or higher-order effects of the residual modes are considered? However, O'Callahan's idea is invalid to consider such higher-order effects.

In this study, we develop a new CMS method under the consideration of higher-order effects of residual modes, leading to further improvements in the accuracy of the CB method. In this formulation, the new generalized coordinate vector is defined by considering the additional coordinates containing the unknown eigenvalues. Employing the concept of system equivalent reduction expansion process (SEREP) [27], the additional unknowns are then eliminated. We name this the higher-order CB (HCB) method.

In the following sections, we will briefly review the CB method, define the residual flexibility, derive the formulation of the HCB method, and present the performance of HCB method through various numerical examples: rectangular plate, cylindrical panel, hyperboloid shell, bent pipe, and automobile wheel problems. The numerical results are compared to the existing CB and ECB methods.

II. Craig–Bampton Method

In the CB method, the global (original) FE model is assembled using N_s substructures connected through a fixed-interface boundary; see Fig. 1. The equations of motion for free vibration without damping are given by

$$\boldsymbol{M}_g\ddot{\boldsymbol{u}}_g + \boldsymbol{K}_g\boldsymbol{u}_g = \boldsymbol{0} \quad \text{with} \quad \boldsymbol{M}_g = \begin{bmatrix} \boldsymbol{M}_s & \boldsymbol{M}_c \\ \boldsymbol{M}_c^T & \boldsymbol{M}_b \end{bmatrix},$$
$$\boldsymbol{K}_g = \begin{bmatrix} \boldsymbol{K}_s & \boldsymbol{K}_c \\ \boldsymbol{K}_c^T & \boldsymbol{K}_b \end{bmatrix}, \qquad \boldsymbol{u}_g = \begin{Bmatrix} \boldsymbol{u}_s \\ \boldsymbol{u}_b \end{Bmatrix} \tag{1}$$

where $\boldsymbol{M}_g$ and $\boldsymbol{K}_g$ are the global mass and stiffness matrices, and $\boldsymbol{u}_g$ is the global displacement vector. The subscripts s and b represent the substructural and interface boundary quantities, respectively, and c represents the coupled quantities between the substructures and interface boundary. The double dot $\ddot{(\,)}$ indicates the second-order differentiation with respect to time t, i.e., $\mathrm{d}^2(\,)/\mathrm{d}t^2$. Here, $\boldsymbol{M}_s$ and $\boldsymbol{K}_s$ are the block-diagonal matrices, and their diagonal component matrices are the substructural mass and stiffness matrices $\boldsymbol{M}_s^{(i)}$ and $\boldsymbol{K}_s^{(i)}$ (for $i = 1, 2, \cdots, N_s$).

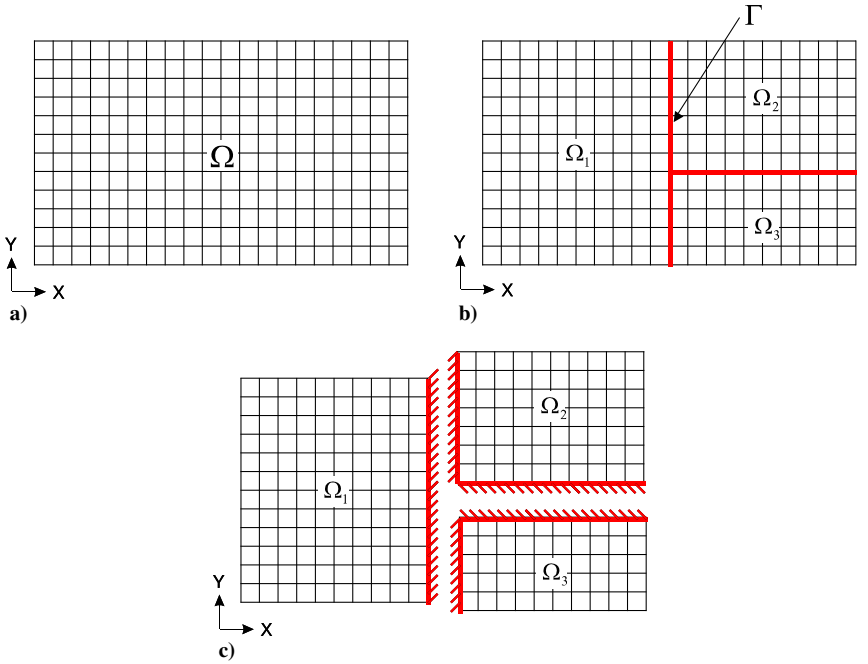

Fig. 1 Partitioning procedures in the Craig–Bampton method: a) global FE model, b) partitioned FE models, and c) fixed-interface boundary.

The global eigenvalue problem is defined as

$$\boldsymbol{K}_g\{\boldsymbol{\varphi}_g\}_j = (\lambda_g)_j \boldsymbol{M}_g\{\boldsymbol{\varphi}_g\}_j \quad \text{for } j = 1, 2, \cdots, N_g \tag{2}$$

in which $(\lambda_g)_j$ and $\{\boldsymbol{\varphi}_g\}_j$ are the global eigenvalue and eigenvector corresponding to the jth global mode, respectively, and N_g is the number of DOFs in the global FE model. Note that, in engineering practice, only a small fraction of the total eigenpairs needs to be considered (for $j = 1, 2, \cdots, p$, where $p \ll N_g$).

In structural dynamics, the square root of the eigenvalue ($\sqrt{\lambda_j}$) and eigenvector are interpreted as a natural frequency ω_j and the corresponding mode shape, respectively. Note that the eigenvectors are scaled to satisfy the following mass-orthonormality condition:

$$\{\boldsymbol{\varphi}_g\}_i^T \boldsymbol{M}_g\{\boldsymbol{\varphi}_g\}_j = \delta_{ij} \quad \text{for } i \text{ and } j = 1, 2, \cdots, N_g \tag{3}$$

where δ_{ij} is the Kronecker delta ($\delta_{ij} = 1$ if $i = j$, otherwise $\delta_{ij} = 0$).

Using the eigenvectors calculated in Eq. (2), the global displacement vector $\boldsymbol{u}_g$ is represented as

$$\boldsymbol{u}_g = \boldsymbol{\Phi}_g \boldsymbol{q}_g,\ \boldsymbol{\Phi}_g = \left[\{\boldsymbol{\varphi}_g\}_1\ \{\boldsymbol{\varphi}_g\}_2\ \cdots\ \{\boldsymbol{\varphi}_g\}_{N_g}\right],\ \boldsymbol{q}_g = \begin{Bmatrix} q_1 \\ q_2 \\ \vdots \\ q_{N_g} \end{Bmatrix} \tag{4}$$

where $\boldsymbol{\Phi}_g$ is the global eigenvector matrix containing the eigenvectors $\{\boldsymbol{\varphi}_g\}_i$, and $\boldsymbol{q}_g$ is the modal coordinate vector containing the modal coordinates q_i corresponding to $\{\boldsymbol{\varphi}_g\}_i$.

In the CB method, the global displacement vector $\boldsymbol{u}_g$ is represented as

$$\boldsymbol{u}_g = \boldsymbol{T}_0 \boldsymbol{u}_0, \qquad \boldsymbol{T}_0 = \begin{bmatrix} \boldsymbol{\Phi}_s & \boldsymbol{\Psi}_c \\ \boldsymbol{0} & \boldsymbol{I}_b \end{bmatrix}, \qquad \boldsymbol{u}_0 = \begin{Bmatrix} \boldsymbol{q}_s \\ \boldsymbol{u}_b \end{Bmatrix} \tag{5}$$

in which $\boldsymbol{T}_0$ and $\boldsymbol{u}_0$ are the global transformation matrix and its generalized coordinate vector, respectively; $\boldsymbol{\Phi}_s$ and $\boldsymbol{\Psi}_c$ are the fixed-interface normal mode and constraint mode matrices, respectively; $\boldsymbol{I}_b$ is the identity matrix for the interface boundary; $\boldsymbol{q}_s$ is the modal coordinate vector corresponding to $\boldsymbol{\Phi}_s$; and $\boldsymbol{u}_b$ is the interface boundary displacement vector.

Note that the matrices $\boldsymbol{\Phi}_s$ and $\boldsymbol{\Psi}_c$ in the global transformation matrix $\boldsymbol{T}_0$ are expressed in a substructural matrix form as

$$\boldsymbol{\Phi}_s = \begin{bmatrix} \boldsymbol{\Phi}_s^{(1)} & & & \boldsymbol{0} \\ & \boldsymbol{\Phi}_s^{(2)} & & \\ & & \ddots & \\ \boldsymbol{0} & & & \boldsymbol{\Phi}_s^{(N_s)} \end{bmatrix},$$

$$\boldsymbol{\Psi}_c = \begin{bmatrix} \boldsymbol{\Psi}_c^{(1)} \\ \boldsymbol{\Psi}_c^{(2)} \\ \vdots \\ \boldsymbol{\Psi}_c^{(N_s)} \end{bmatrix} \quad \text{with} \quad \boldsymbol{\Psi}_c^{(i)} = -\left(\boldsymbol{K}_s^{(i)}\right)^{-1} \boldsymbol{K}_c \tag{6}$$

The diagonal component matrices of $\boldsymbol{\Phi}_s$ in Eq. (6) can be obtained by solving the following substructural eigenvalue problems:

$$\boldsymbol{K}_s^{(i)} \boldsymbol{\Phi}_s^{(i)} = \boldsymbol{\Lambda}_s^{(i)} \boldsymbol{M}_s^{(i)} \boldsymbol{\Phi}_s^{(i)}, \quad \boldsymbol{\Phi}_s^{(i)} = \begin{bmatrix} \boldsymbol{\Phi}_d^{(i)} & \boldsymbol{\Phi}_r^{(i)} \end{bmatrix}$$
$$\text{for } i = 1, 2, \cdots, N_s \tag{7}$$

where $\boldsymbol{\Phi}_s^{(i)}$ and $\boldsymbol{\Lambda}_s^{(i)}$ are the substructural eigenvector and eigenvalue matrices corresponding to the ith substructure, and the substructural eigenvector matrix $\boldsymbol{\Phi}_s^{(i)}$ is divided into the dominant term $\boldsymbol{\Phi}_d^{(i)}$ and residual term $\boldsymbol{\Phi}_r^{(i)}$. The subscripts d and r denote the dominant and residual quantities. Note that, in the substructural eigenvalue problems, a small fraction of the total substructural eigenpairs is calculated.

Using the substructural eigenvector matrices $\boldsymbol{\Phi}_d^{(i)}$ and $\boldsymbol{\Phi}_r^{(i)}$, the fixed-interface normal modes matrix $\boldsymbol{\Phi}_s$ can be reordered as

$$\boldsymbol{\Phi}_s = \begin{bmatrix} \boldsymbol{\Phi}_d & \boldsymbol{\Phi}_r \end{bmatrix} \tag{8}$$

in which $\boldsymbol{\Phi}_d$ and $\boldsymbol{\Phi}_r$ are the dominant and residual eigenvector matrices, respectively, and these matrices are the block-diagonal matrices, in which diagonal terms consist of the substructural eigenvector matrices, $\boldsymbol{\Phi}_d^{(i)}$ and $\boldsymbol{\Phi}_r^{(i)}$, described in Eq. (7).

Substituting Eq. (8) into Eq. (5), the global displacement vector $\boldsymbol{u}_g$ is represented as

$$\boldsymbol{u}_g = \begin{Bmatrix} \boldsymbol{u}_s \\ \boldsymbol{u}_b \end{Bmatrix} = \boldsymbol{T}_0 \boldsymbol{u}_0 \text{ with } \boldsymbol{T}_0 = \begin{bmatrix} \boldsymbol{\Phi}_d & \boldsymbol{\Phi}_r & \boldsymbol{\Psi}_c \\ \boldsymbol{0} & \boldsymbol{0} & \boldsymbol{I}_b \end{bmatrix}, \ \boldsymbol{u}_0 = \begin{Bmatrix} \boldsymbol{q}_d \\ \boldsymbol{q}_r \\ \boldsymbol{u}_b \end{Bmatrix} \tag{9}$$

in which $\boldsymbol{q}_d$ and $\boldsymbol{q}_r$ are the modal coordinates vectors corresponding to $\boldsymbol{\Phi}_d$ and $\boldsymbol{\Phi}_r$, respectively.

Truncating the residual eigenvector matrix $\boldsymbol{\Phi}_r$ and the corresponding modal coordinate vector $\boldsymbol{q}_r$ in Eq. (9), the approximated global displacement vector $\bar{\boldsymbol{u}}_g$ is obtained:

$$\boldsymbol{u}_g \approx \bar{\boldsymbol{u}}_g = \begin{Bmatrix} \bar{\boldsymbol{u}}_s \\ \boldsymbol{u}_b \end{Bmatrix} = \bar{\boldsymbol{T}}_0 \bar{\boldsymbol{u}}_0, \quad \bar{\boldsymbol{T}}_0 = \begin{bmatrix} \boldsymbol{\Phi}_d & \boldsymbol{\Psi}_c \\ \boldsymbol{0} & \boldsymbol{I}_b \end{bmatrix}, \quad \bar{\boldsymbol{u}}_0 = \begin{Bmatrix} \boldsymbol{q}_d \\ \boldsymbol{u}_b \end{Bmatrix} \tag{10}$$

where $\bar{\boldsymbol{T}}_0$ and $\bar{\boldsymbol{u}}_0$ are the CB transformation matrix ($N_g \times \bar{N}_0$) and the corresponding generalized coordinate vector, respectively. $\bar{N}_0$ is the number of DOFs in the reduced FE model; $\bar{N}_0 = N_d + N_b$ with

$$N_d = \sum_{i=1}^{N_s} N_d^{(i)}$$

where $N_d^{(i)}$ is the number of dominant modes of the ith substructure, and N_b is the number of DOFs on the interface boundary. The overbar $\bar{(\ )}$ denotes the approximated quantity. Note that the residual eigenvector matrix $\boldsymbol{\Phi}_r$ is simply truncated without any consideration.

Using the transformation matrix $\bar{\boldsymbol{T}}_0$ in Eq. (10), the reduced equations of motion are

$$\bar{\boldsymbol{M}}_0 \ddot{\bar{\boldsymbol{u}}}_0 + \bar{\boldsymbol{K}}_0 \bar{\boldsymbol{u}}_0 = 0 \text{ with } \bar{\boldsymbol{M}}_0 = \bar{\boldsymbol{T}}_0^T \boldsymbol{M}_g \bar{\boldsymbol{T}}_0, \ \bar{\boldsymbol{K}}_0 = \bar{\boldsymbol{T}}_0^T \boldsymbol{K}_g \bar{\boldsymbol{T}}_0 \tag{11}$$

in which $\bar{\boldsymbol{M}}_0$ and $\bar{\boldsymbol{K}}_0$ are the reduced mass and stiffness matrices ($\bar{N}_0 \times \bar{N}_0$), respectively.

Using $\bar{\boldsymbol{M}}_0$ and $\bar{\boldsymbol{K}}_0$ in Eq. (11), the reduced eigenvalue problem is given by

$$\bar{\boldsymbol{K}}_0 \{\bar{\boldsymbol{\varphi}}_0\}_j = (\bar{\lambda}_0)_j \bar{\boldsymbol{M}}_0 \{\bar{\boldsymbol{\varphi}}_0\}_j \quad \text{for } j = 1, 2, \cdots, \bar{N}_0 \tag{12}$$

and the approximated eigenvector matrix $\bar{\boldsymbol{\Phi}}_0$ is defined as

$$\bar{\boldsymbol{\Phi}}_0 = \begin{bmatrix} \{\bar{\boldsymbol{\varphi}}_0\}_1 & \{\bar{\boldsymbol{\varphi}}_0\}_2 & \cdots & \{\bar{\boldsymbol{\varphi}}_0\}_j \end{bmatrix} \text{ for } j = 1, 2, \cdots, \bar{N}_0 \tag{13}$$

where $(\bar{\lambda}_0)_j$ and $\{\bar{\boldsymbol{\varphi}}_0\}_j$ are the jth approximated eigenvalue and eigenvector.

The reduced displacement vector $\bar{\boldsymbol{u}}_0$ is then represented by

$$\bar{\boldsymbol{u}}_0 = \bar{\boldsymbol{\Phi}}_0 \bar{\boldsymbol{q}}_0 \tag{14}$$

where $\bar{\boldsymbol{q}}_0$ is the modal coordinate vector corresponding to $\bar{\boldsymbol{\Phi}}_0$, and the approximated global eigenvector matrix $\bar{\boldsymbol{\Phi}}_g$ is obtained by

$$\bar{\boldsymbol{\Phi}}_g = \bar{\boldsymbol{T}}_0 \bar{\boldsymbol{\Phi}}_0, \quad \{\boldsymbol{\varphi}_g\}_j = \bar{\boldsymbol{T}}_0 \{\bar{\boldsymbol{\varphi}}_0\}_j \quad \text{for } j = 1, 2, \cdots, \bar{N}_0 \tag{15}$$

III. Higher-Order Craig–Bampton Method

In this section, we derive the formulation of the higher-order CB (HCB) method, in which the residual eigenvector matrix $\boldsymbol{\Phi}_r$ is properly considered to construct the reduced model more accurately.

Using $\boldsymbol{T}_0$ in Eq. (9), the equations of motion in Eq. (1) are transformed into

$$\left[\frac{\mathrm{d}^2}{\mathrm{d}t^2}\boldsymbol{M}_0 + \boldsymbol{K}_0\right]\boldsymbol{u}_0 = \boldsymbol{0} \tag{16a}$$

$$\boldsymbol{M}_0 = \boldsymbol{T}_0^T \boldsymbol{M}_g \boldsymbol{T}_0 = \begin{bmatrix} \boldsymbol{I}_d & \boldsymbol{0} & \boldsymbol{\Phi}_d^T \hat{\boldsymbol{M}}_c \\ \boldsymbol{0} & \boldsymbol{I}_r & \boldsymbol{\Phi}_r^T \hat{\boldsymbol{M}}_c \\ \hat{\boldsymbol{M}}_c^T \boldsymbol{\Phi}_d & \hat{\boldsymbol{M}}_c^T \boldsymbol{\Phi}_r & \hat{\boldsymbol{M}}_b \end{bmatrix},$$

$$\boldsymbol{K}_0 = \boldsymbol{T}_0^T \boldsymbol{K}_g \boldsymbol{T}_0 = \begin{bmatrix} \boldsymbol{\Lambda}_d & \boldsymbol{0} & \boldsymbol{0} \\ \boldsymbol{0} & \boldsymbol{\Lambda}_r & \boldsymbol{0} \\ \boldsymbol{0} & \boldsymbol{0} & \hat{\boldsymbol{K}}_b \end{bmatrix} \tag{16b}$$

where $\boldsymbol{M}_0$ and $\boldsymbol{K}_0$ are the transformed global mass and stiffness matrices, respectively, and the component matrices in Eq. (16b) are defined by

$$\boldsymbol{I}_d = \boldsymbol{\Phi}_d^T \boldsymbol{M}_s \boldsymbol{\Phi}_d, \qquad \boldsymbol{I}_r = \boldsymbol{\Phi}_r^T \boldsymbol{M}_s \boldsymbol{\Phi}_r \tag{17a}$$

$$\boldsymbol{\Lambda}_d = \boldsymbol{\Phi}_d^T \boldsymbol{K}_s \boldsymbol{\Phi}_d, \qquad \boldsymbol{\Lambda}_r = \boldsymbol{\Phi}_r^T \boldsymbol{K}_s \boldsymbol{\Phi}_r \tag{17b}$$

$$\hat{\boldsymbol{M}}_c = \boldsymbol{M}_c + \boldsymbol{M}_s \boldsymbol{\Psi}_c, \ \ \hat{\boldsymbol{M}}_b = \boldsymbol{M}_b + \boldsymbol{\Psi}_c^T \boldsymbol{M}_c + \boldsymbol{M}_c^T \boldsymbol{\Psi}_c + \boldsymbol{\Psi}_c^T \boldsymbol{M}_s \boldsymbol{\Psi}_c \tag{17c}$$

$$\hat{\boldsymbol{K}}_b = \boldsymbol{K}_b + \boldsymbol{K}_c^T \boldsymbol{\Psi}_c \tag{17d}$$

Considering a harmonic response $[\mathrm{d}^2(\,)/\mathrm{d}t^2 = -\lambda]$, Eq. (16) can be rewritten as

$$\begin{bmatrix} \boldsymbol{\Lambda}_d - \lambda \boldsymbol{I}_d & \boldsymbol{0} & -\lambda \boldsymbol{\Phi}_d^T \hat{\boldsymbol{M}}_c \\ \boldsymbol{0} & \boldsymbol{\Lambda}_r - \lambda \boldsymbol{I}_r & -\lambda \boldsymbol{\Phi}_r^T \hat{\boldsymbol{M}}_c \\ -\lambda \hat{\boldsymbol{M}}_c^T \boldsymbol{\Phi}_d & -\lambda \hat{\boldsymbol{M}}_c^T \boldsymbol{\Phi}_r & \hat{\boldsymbol{K}}_b - \lambda \hat{\boldsymbol{M}}_b \end{bmatrix} \begin{Bmatrix} \boldsymbol{q}_d \\ \boldsymbol{q}_r \\ \boldsymbol{u}_b \end{Bmatrix} = \boldsymbol{0} \tag{18}$$

and, from the second row in Eq. (18), the following equation is obtained:

$$\boldsymbol{q}_r = \lambda [\boldsymbol{\Lambda}_r - \lambda \boldsymbol{I}_r]^{-1} \boldsymbol{\Phi}_r^T \hat{\boldsymbol{M}}_c \boldsymbol{u}_b \tag{19}$$

Substituting Eq. (19) into Eq. (9), the global displacement vector $\boldsymbol{u}_g$ can be represent as

$$\boldsymbol{u}_g = \begin{Bmatrix} \boldsymbol{u}_s \\ \boldsymbol{u}_b \end{Bmatrix} = \boldsymbol{T}_0 \boldsymbol{u}_0 \quad \text{with}$$

$$\boldsymbol{T}_0 = \begin{bmatrix} \boldsymbol{\Phi}_d & \boldsymbol{\Psi}_c + \lambda \boldsymbol{\Phi}_r [\boldsymbol{\Lambda}_r - \lambda \boldsymbol{I}_r]^{-1} \boldsymbol{\Phi}_r^T \hat{\boldsymbol{M}}_c \\ \boldsymbol{0} & \boldsymbol{I}_b \end{bmatrix}, \ \boldsymbol{u}_0 = \begin{Bmatrix} \boldsymbol{q}_d \\ \boldsymbol{u}_b \end{Bmatrix} \tag{20}$$

In Eq. (20), the residual flexibility $\boldsymbol{\Phi}_r [\boldsymbol{\Lambda}_r - \lambda \boldsymbol{I}_r]^{-1} \boldsymbol{\Phi}_r^T$ can be expanded by using Taylor series [17,19,21,22]:

$$\boldsymbol{\Phi}_r [\boldsymbol{\Lambda}_r - \lambda \boldsymbol{I}_r]^{-1} \boldsymbol{\Phi}_r^T = \boldsymbol{F}_1 + \lambda^1 \boldsymbol{F}_2 + \cdots \lambda^{i-1} \boldsymbol{F}_i + \cdots \quad \text{with}$$
$$\boldsymbol{F}_i = \boldsymbol{\Phi}_r \boldsymbol{\Lambda}_r^{-i} \boldsymbol{\Phi}_r^T \tag{21}$$

where $\boldsymbol{F}_i$ is the ith-order residual flexibility matrix.

It should be noted that, through the Neumann series expansion theorem [28], the expansion in Eq. (21) is valid if the eigenvalue λ is smaller than the smallest eigenvalue of $\boldsymbol{\Lambda}_r$, which is the residual eigenvalue matrix for substructures. In the CB method, this expansion is generally valid because the dominant substructural modes are selected to reflect lower modes of the original FE model [4].

Without using the residual modes, the residual flexibility matrix $\boldsymbol{F}_i$ is indirectly calculated by

$$\boldsymbol{F}_i = \boldsymbol{K}_s^{-i} - \boldsymbol{\Phi}_d \boldsymbol{\Lambda}_d^{-i} \boldsymbol{\Phi}_d^T \tag{22}$$

It is important to note that, as the order i increases, $\boldsymbol{K}_s^{-i}$ and $\boldsymbol{\Phi}_d\boldsymbol{\Lambda}_d^{-i}\boldsymbol{\Phi}_d^T$ rapidly approach one another. This results in a loss of precision in the computation of $\boldsymbol{F}_i$. Therefore, for the precise calculation of $\boldsymbol{F}_i$, the number of significant digits used must be properly chosen. This issue will be studied through a numerical example in Sec. IV.A.

Considering the nth-order approximation of the residual flexibility

$$\boldsymbol{\Phi}_r[\boldsymbol{\Lambda}_r - \lambda\boldsymbol{I}_r]^{-1}\boldsymbol{\Phi}_r^T \approx \boldsymbol{F}_1 + \lambda^1\boldsymbol{F}_2 + \cdots + \lambda^{n-1}\boldsymbol{F}_n \tag{23}$$

and substituting it into Eq. (20), the nth-order approximation of the global displacement vector $\boldsymbol{u}_g$ is given by

$$\boldsymbol{u}_g \approx \bar{\boldsymbol{u}}_g = \begin{Bmatrix} \bar{\boldsymbol{u}}_s \\ \boldsymbol{u}_b \end{Bmatrix} = \hat{\boldsymbol{T}}_n\bar{\boldsymbol{u}}_n \quad \text{with}$$

$$\hat{\boldsymbol{T}}_n = \left[\begin{array}{cc|c|ccc} \boldsymbol{\Phi}_d & \boldsymbol{\Psi}_c & \hat{\boldsymbol{\Theta}}_1 & \cdots & \hat{\boldsymbol{\Theta}}_n \\ \boldsymbol{0} & \boldsymbol{I}_b & \boldsymbol{0} & \cdots & \boldsymbol{0} \end{array}\right], \qquad \bar{\boldsymbol{u}}_n = \begin{Bmatrix} \boldsymbol{q}_d \\ \boldsymbol{u}_b \\ \hline \boldsymbol{\eta}_1 \\ \vdots \\ \boldsymbol{\eta}_n \end{Bmatrix}$$

$$\hat{\boldsymbol{\Theta}}_n = \boldsymbol{F}_n\hat{\boldsymbol{M}}_c, \qquad \boldsymbol{\eta}_n = \lambda^n\boldsymbol{u}_b \tag{24}$$

where $\hat{\boldsymbol{T}}_n$ and $\bar{\boldsymbol{u}}_n$ are the HCB transformation matrix ($N_g \times \bar{N}_n$) and the corresponding generalized coordinate vector, respectively. $\bar{N}_n$ is the number of DOFs in the reduced FE model ($\bar{N}_n = N_d + N_b \times n$), $\hat{\boldsymbol{\Theta}}_n$ is the residual mode matrix containing the nth-order residual flexibility $\boldsymbol{F}_n$, and $\boldsymbol{\eta}_n$ is the additional coordinate vector containing the unknown eigenvalue λ^n. Note that the zeroth-order transformation matrix ($n = 0$) is nothing but the CB transformation matrix $\bar{\boldsymbol{T}}_0$ in Eq. (10).

As mentioned already, $\boldsymbol{\Phi}_d$ has been normalized with respect to $\boldsymbol{M}_s$. On the other hand, $\hat{\boldsymbol{\Theta}}_n$ has an arbitrary amplitude without normalization. Thus, $\hat{\boldsymbol{\Theta}}_n$ needs to be properly normalized. Otherwise, $\hat{\boldsymbol{\Theta}}_n$ may produce a badly scaled transformation matrix, which results in ill-conditioned reduced stiffness and mass matrices. We normalize each column of $\hat{\boldsymbol{\Theta}}_n$ using its L2-norm [29,30]:

$$\boldsymbol{\Theta}_n = \hat{\boldsymbol{\Theta}}_n\boldsymbol{G}_n^{-1} \text{ with } \boldsymbol{G}_n = \begin{bmatrix} \|\{\boldsymbol{\theta}_n\}_1\|_2 & & & \boldsymbol{0} \\ & \|\{\boldsymbol{\theta}_n\}_2\|_2 & & \\ & & \ddots & \\ \boldsymbol{0} & & & \|\{\boldsymbol{\theta}_n\}_{N_b}\|_2 \end{bmatrix} \tag{25}$$

where $\boldsymbol{\Theta}_n$ is the normalized residual mode matrix containing the nth-order residual flexibility, and $\{\boldsymbol{\theta}_n\}_j$ is the jth column vector of $\hat{\boldsymbol{\Theta}}_n$.

For the nth-order HCB method, the global displacement vector $\boldsymbol{u}_g$ can be approximated by

$$\boldsymbol{u}_g \approx \bar{\boldsymbol{u}}_g = \begin{Bmatrix} \bar{\boldsymbol{u}}_s \\ \boldsymbol{u}_b \end{Bmatrix} = \bar{\boldsymbol{T}}_n\bar{\boldsymbol{u}}_n \quad \text{with}$$

$$\bar{\boldsymbol{T}}_n = \left[\begin{array}{cc|c|ccc} \boldsymbol{\Phi}_d & \boldsymbol{\Psi}_c & \boldsymbol{\Theta}_1 & \cdots & \boldsymbol{\Theta}_n \\ \boldsymbol{0} & \boldsymbol{I}_b & \boldsymbol{0} & \cdots & \boldsymbol{0} \end{array}\right], \quad \bar{\boldsymbol{u}}_n = \begin{Bmatrix} \boldsymbol{q}_d \\ \boldsymbol{u}_b \\ \hline \boldsymbol{\eta}_1 \\ \vdots \\ \boldsymbol{\eta}_n \end{Bmatrix} \tag{26}$$

where $\bar{\boldsymbol{T}}_n$ and $\bar{\boldsymbol{u}}_n$ are the nth-order HCB transformation matrix ($N_g \times \bar{N}_n$) and the corresponding generalized coordinate vector, respectively.

Using $\bar{\boldsymbol{T}}_n$ in Eq. (26), the following reduced equations of motion are obtained:

$$\bar{\boldsymbol{M}}_n\ddot{\bar{\boldsymbol{u}}}_n + \bar{\boldsymbol{K}}_n\bar{\boldsymbol{u}}_n = \boldsymbol{0} \quad \text{with} \quad \bar{\boldsymbol{M}}_n = \bar{\boldsymbol{T}}_n^T\boldsymbol{M}_g\bar{\boldsymbol{T}}_n, \quad \bar{\boldsymbol{K}}_n = \bar{\boldsymbol{T}}_n^T\boldsymbol{K}_g\bar{\boldsymbol{T}}_n \tag{27}$$

in which $\bar{\boldsymbol{M}}_n$ and $\bar{\boldsymbol{K}}_n$ are the reduced mass and stiffness matrices ($\bar{N}_n \times \bar{N}_n$). Note that the reduced system in Eq. (27) has larger size than the system reduced by the original CB method in Eq. (11) due to the use of additional generalized coordinates.

The additional coordinates can be eliminated by employing the concept of SEREP [27], which is a DOF-based reduction method without accuracy loss. Then, the reduced system in Eq. (27) can be further reduced, leading to the same number of equations of motion reduced by the original CB method in Eq. (11). However, this procedure increases computation time inevitably.

From Eq. (27), the following eigenvalue problem is obtained:

$$\bar{\boldsymbol{K}}_n\{\bar{\boldsymbol{\varphi}}_n\}_j = (\bar{\lambda}_n)_j\bar{\boldsymbol{M}}_n\{\bar{\boldsymbol{\varphi}}_n\}_j \quad \text{for } j = 1, 2, \cdots, \bar{N}_n \tag{28}$$

where $(\bar{\lambda}_n)_j$ and $\{\boldsymbol{\varphi}_n\}_j$ are the eigenvalue and eigenvector, respectively.

We then calculate the eigenvectors up to the $\bar{N}_0$th mode and construct the following eigenvector matrix:

$$\boldsymbol{\Phi}_n = \begin{bmatrix} \{\bar{\boldsymbol{\varphi}}_n\}_1 & \{\bar{\boldsymbol{\varphi}}_n\}_2 & \cdots & \{\bar{\boldsymbol{\varphi}}_n\}_{\bar{N}_0} \end{bmatrix} \tag{29}$$

Using the eigenvector matrix in Eq. (29), the transformation matrix $\bar{\boldsymbol{T}}_n$ is reduced as

$$\tilde{\boldsymbol{T}}_n = \bar{\boldsymbol{T}}_n\boldsymbol{\Phi}_n \tag{30}$$

where $\tilde{\boldsymbol{T}}_n$ is the reduced transformation matrix of the HCB method, the size of which is the same as that of $\bar{\boldsymbol{T}}_0$ ($N_g \times \bar{N}_0$).

Finally, the reduced matrices constructed by the HCB method are obtained:

$$\tilde{\boldsymbol{M}}_n = \tilde{\boldsymbol{T}}_n^T\boldsymbol{M}_g\tilde{\boldsymbol{T}}_n, \qquad \tilde{\boldsymbol{K}}_n = \tilde{\boldsymbol{T}}_n^T\boldsymbol{K}_g\tilde{\boldsymbol{T}}_n \tag{31}$$

in which $\tilde{\boldsymbol{M}}_n$ and $\tilde{\boldsymbol{K}}_n$ are the reduced mass and stiffness matrices of size $\bar{N}_0 \times \bar{N}_0$.

The reduced eigenvalue problem in the HCB method is also defined by

$$\tilde{\boldsymbol{K}}_n\{\tilde{\boldsymbol{\varphi}}_n\}_j = (\tilde{\lambda}_n)_j\tilde{\boldsymbol{M}}_n\{\tilde{\boldsymbol{\varphi}}_n\}_j \quad \text{for } j = 1, 2, \cdots, \bar{N}_0 \tag{32}$$

where $(\tilde{\lambda}_n)_j$ and $\{\tilde{\boldsymbol{\varphi}}_n\}_j$ are the approximated eigenvalues and eigenvectors, respectively.

As the order of residual flexibility considered in the formulation increases, the reduced system becomes more accurate. Various orders of the HCB methods can be defined depending on the order

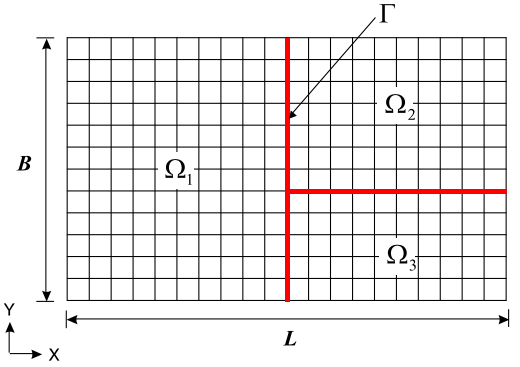

Fig. 2 Rectangular plate problem (20 × 12 mesh, three substructures).

Table 1 Numbers of dominant modes selected for the rectangular plate problem

$N_d^{(1)}$	$N_d^{(2)}$	$N_d^{(3)}$	N_d	N_g
13	7	5	25	1365

considered. Here, we define the nth-order HCB method (denoted HCB-n), in which the nth-order HCB transformation matrix is used. Note that HCB-0 is equivalent to the original CB method.

IV. Numerical Examples

In this section, we compare the performance of the present method (HCB) with two previous methods: the original CB method (CB) and the enhanced CB method (ECB). Four structural problems are considered: rectangular plate, cylindrical panel, hyperboloid shell, and bent pipe problems. The component mode synthesis methods are implemented in MATLAB, and computation is performed on a personal computer (Intel Core i7-3770, 3.40 GHz CPU, 32 GB RAM). The well-known frequency cutoff criterion [31] is adopted to select substructural dominant modes.

To measure the accuracy of the reduced models constructed by different methods, the following relative eigenvalue errors are calculated:

$$\xi_j = \frac{|\lambda_j - \bar{\lambda}_j|}{\lambda_j} \tag{33}$$

where ξ_j is the jth relative eigenvalue error, λ_j is the jth exact eigenvalue calculated from the global (original) eigenvalue problem in Eq. (2), and $\bar{\lambda}_j$ is the jth approximated eigenvalue calculated from the reduced eigenvalue problem. Note that rigid-body modes are not considered in measuring the accuracy.

A. Rectangular Plate Problem

Consider a rectangular plate with free boundary in Fig. 2. Its length L is 20.0 m, width B is 12.0 m, and thickness h is 0.08 m. Young's modulus E is 206 GPa, Poisson's ratio ν is 0.33, and density $\boldsymbol{\rho}$ is 7850 kg/m^3. The plate structure is modeled by a 20×12 mesh of the four-node mixed interpolation of tensorial components (MITC) shell elements [32–35] and partitioned into three substructures ($N_s = 3$). The number of DOFs for this problem is 1365 ($N_g = 1365$).

We select 25 dominant modes ($N_d = 25$). The number of modes selected in each substructure ($N_d^{(k)}$) is listed in Table 1. Using four HCB methods (HCB-0, HCB-1, HCB-2, and HCB-3), we construct reduced models. The four methods are implemented with two different numbers of significant digits, namely 16 and 32.

Figures 3a and 3b present the relative eigenvalue errors obtained by the four HCB methods using 16 and 32 significant digits, respectively. When 16 significant digits are used for computation, the accuracy of the HCB-3 method deteriorates due to the loss of

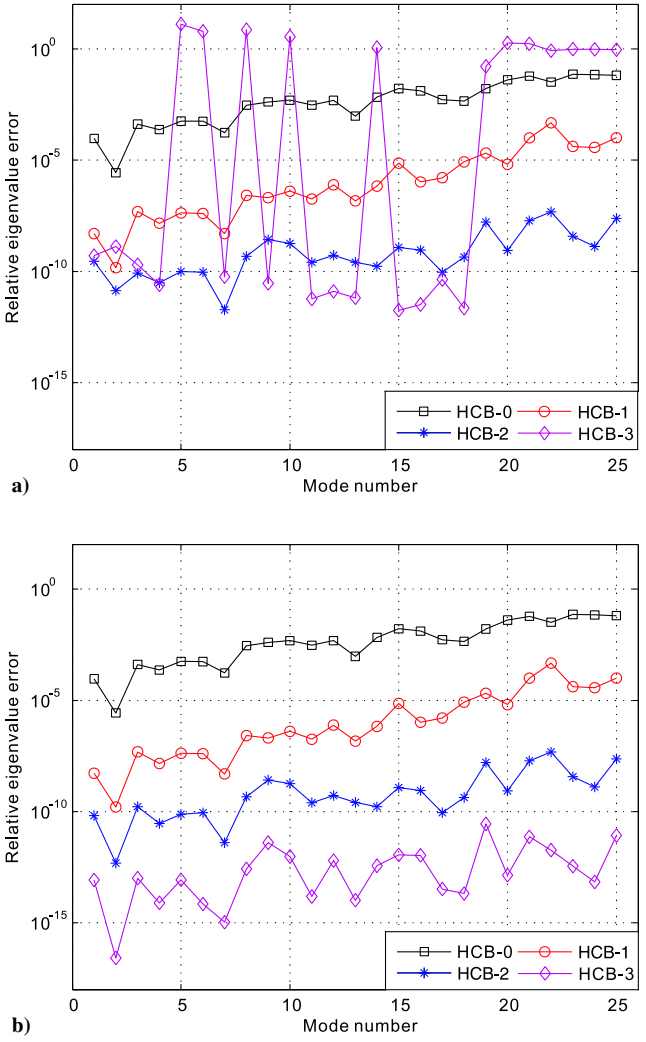

Fig. 3 Relative eigenvalue errors for the rectangular plate problem (20×12 mesh, three substructures, $N_d = 25$): a) 16 significant digits, and b) 32 significant digits.

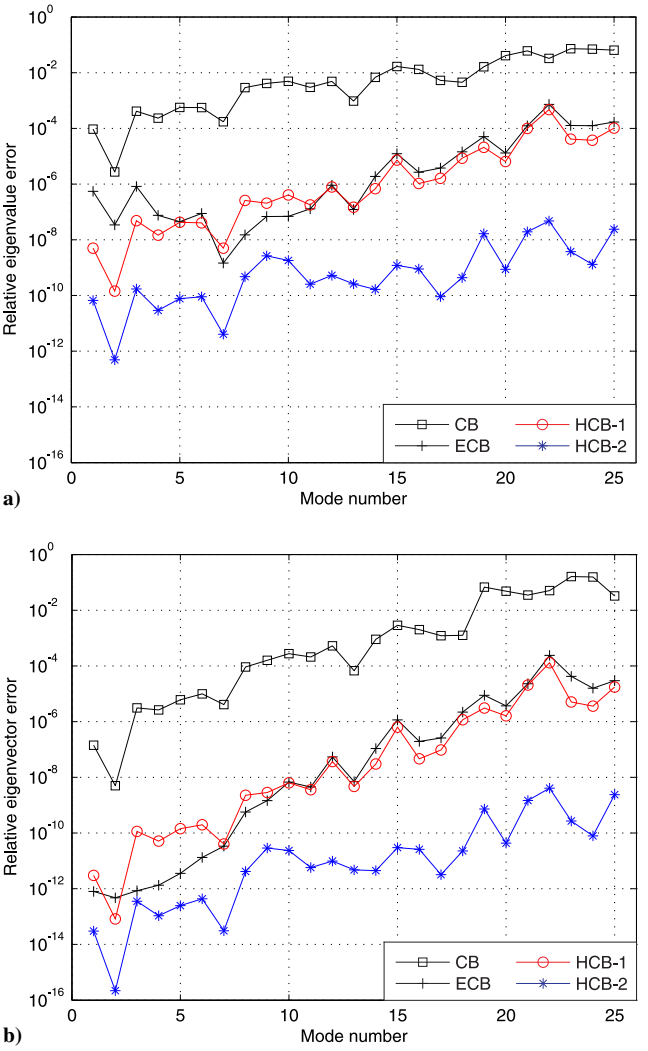

Fig. 4 Errors for the rectangular plate problem (20×12 mesh, three substructures, $N_d = 25$): a) relative eigenvalue errors, and b) relative eigenvector errors.

Table 2 Relative eigenvalue errors for the rectangular plate problem

			Present	
Mode number	CB	ECB	HCB-1	HCB-2
1	9.415E-05	5.002E-07	5.005E-09	2.959E-10
2	2.728E-06	8.761E-09	1.427E-10	1.950E-11
3	4.116E-04	2.025E-07	4.866E-08	8.009E-11
4	2.340E-04	2.197E-08	1.457E-08	2.506E-11
5	5.675E-04	4.546E-08	4.259E-08	9.764E-11
6	5.586E-04	1.249E-08	4.047E-08	9.358E-11
7	1.717E-04	2.960E-09	5.021E-09	1.588E-12
8	2.912E-03	1.219E-08	2.600E-07	4.676E-10
9	4.129E-03	6.508E-08	2.054E-07	2.649E-09
10	4.914E-03	1.323E-07	4.067E-07	1.798E-09
11	2.972E-03	1.375E-07	1.792E-07	2.574E-10
12	4.866E-03	9.119E-07	7.829E-07	5.316E-10
13	9.609E-04	1.271E-07	1.477E-07	2.608E-10
14	6.775E-03	1.882E-06	6.818E-07	1.666E-10
15	1.662E-02	1.236E-05	7.281E-06	1.207E-09
16	1.306E-02	2.638E-06	1.051E-06	8.905E-10
17	5.277E-03	3.759E-06	1.610E-06	9.068E-11
18	4.522E-03	1.441E-05	8.445E-06	4.373E-10
19	1.627E-02	5.038E-05	2.083E-05	1.653E-08
20	4.090E-02	1.305E-05	6.466E-06	8.669E-10
21	6.032E-02	1.227E-04	1.002E-04	1.923E-08
22	3.275E-02	7.298E-04	4.724E-04	4.747E-08
23	7.284E-02	1.260E-04	4.135E-05	3.747E-09
24	7.013E-02	1.250E-04	3.734E-05	1.310E-09
25	6.422E-02	1.694E-04	1.021E-04	2.382E-08

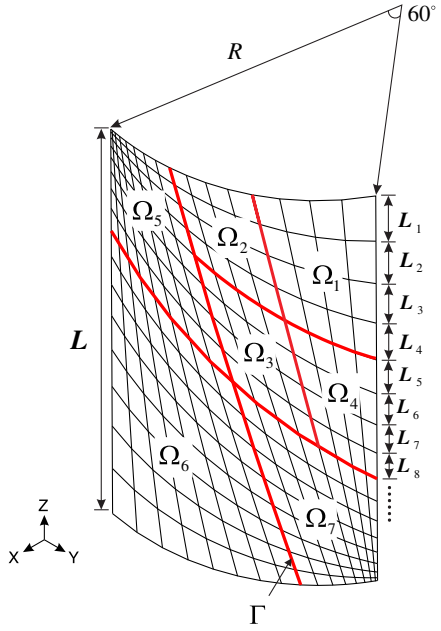

Fig. 5 Cylindrical panel problem with a distorted mesh.

precision in the computation of $\boldsymbol{F}_i$. However, when 32 significant decimal digits are used, the accuracy deterioration phenomenon disappears. Because 16 significant digits are usually employed in engineering computations, this problem must be resolved in future work.

Table 3 Number of dominant modes selected for the cylindrical panel problem

Case	$N_d^{(1)}$	$N_d^{(2)}$	$N_d^{(3)}$	$N_d^{(4)}$	$N_d^{(5)}$	$N_d^{(6)}$	$N_d^{(7)}$	N_d	N_g
1	2	2	2	2	4	4	4	20	1445
2	4	4	4	4	8	8	8	40	1445

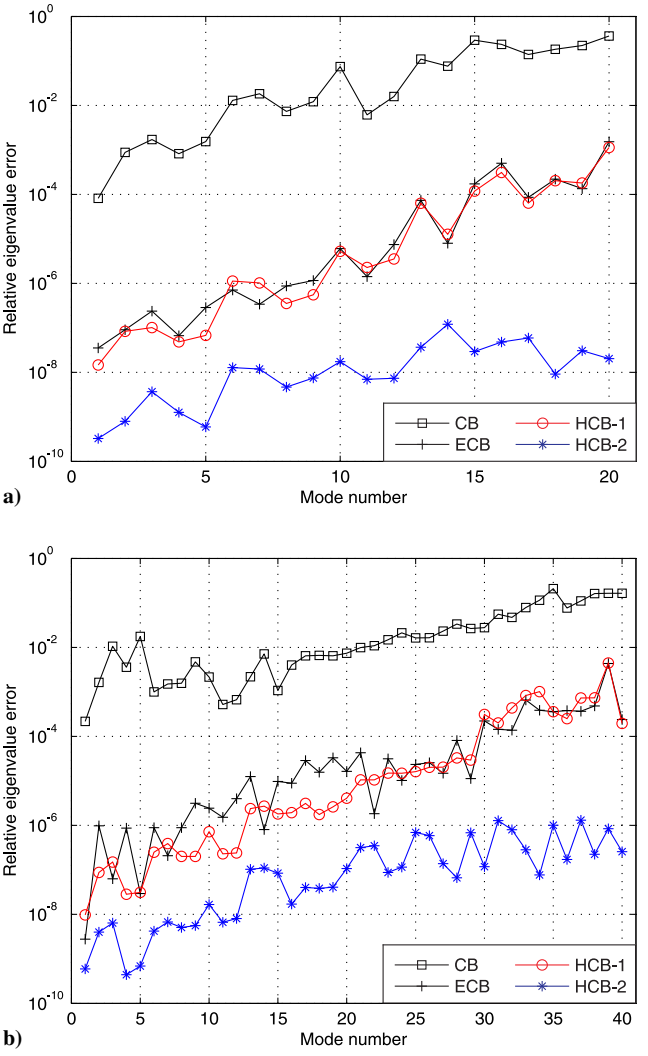

Fig. 6 Relative eigenvalue errors for the cylindrical panel problem: a) $N_d = 20$, and b) $N_d = 40$.

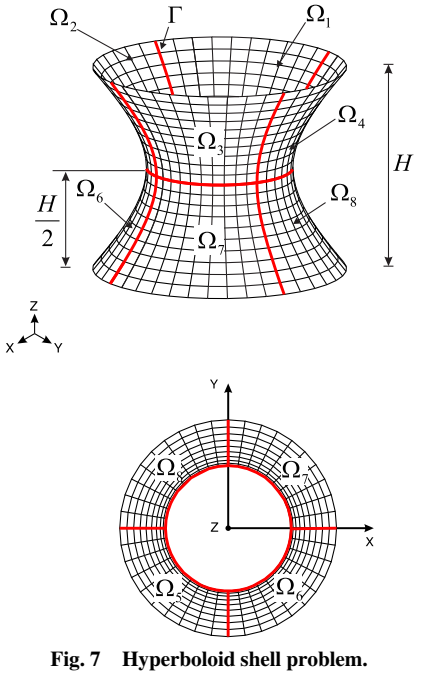

Fig. 7 Hyperboloid shell problem.

Table 4 Numbers of dominant modes selected for the hyperboloid shell problem

Case	$N_d^{(1)}$	$N_d^{(2)}$	$N_d^{(3)}$	$N_d^{(4)}$	$N_d^{(5)}$	$N_d^{(6)}$	$N_d^{(7)}$	$N_d^{(8)}$	N_d	N_g
1	3	3	3	3	3	3	3	3	24	4200
2	4	4	4	4	4	4	4	4	32	4200

After this point, we use only 16 significant digits in computation due to the large amount of computation time required for 32 significant digits. Figure 4a and Table 2 present the relative eigenvalue errors in reduced models constructed by the CB, ECB, HCB-1, and HCB-2 methods.

Figure 4b presents the relative eigenvector errors defined using MAC (modal assurance criterion) [36]

$$\zeta_i = 1 - \frac{|\boldsymbol{\varphi}_i \cdot \bar{\boldsymbol{\varphi}}_i|}{\|\boldsymbol{\varphi}_i\|_2 \|\bar{\boldsymbol{\varphi}}_i\|_2} \tag{34}$$

where ζ_i is the ith relative eigenvector error, $\boldsymbol{\varphi}_i$ is the ith exact eigenvector calculated from the global (original) eigenvalue problem in Eq. (2), and $\bar{\boldsymbol{\varphi}}_i$ is the ith approximated eigenvector obtained from the reduced eigenvalue problem.

The results in Fig. 4 show that the accuracy of the HCB-1 method is similar to that of the ECB method, and the HCB-2 method provides further improved accuracy, in particular, in relatively higher modes.

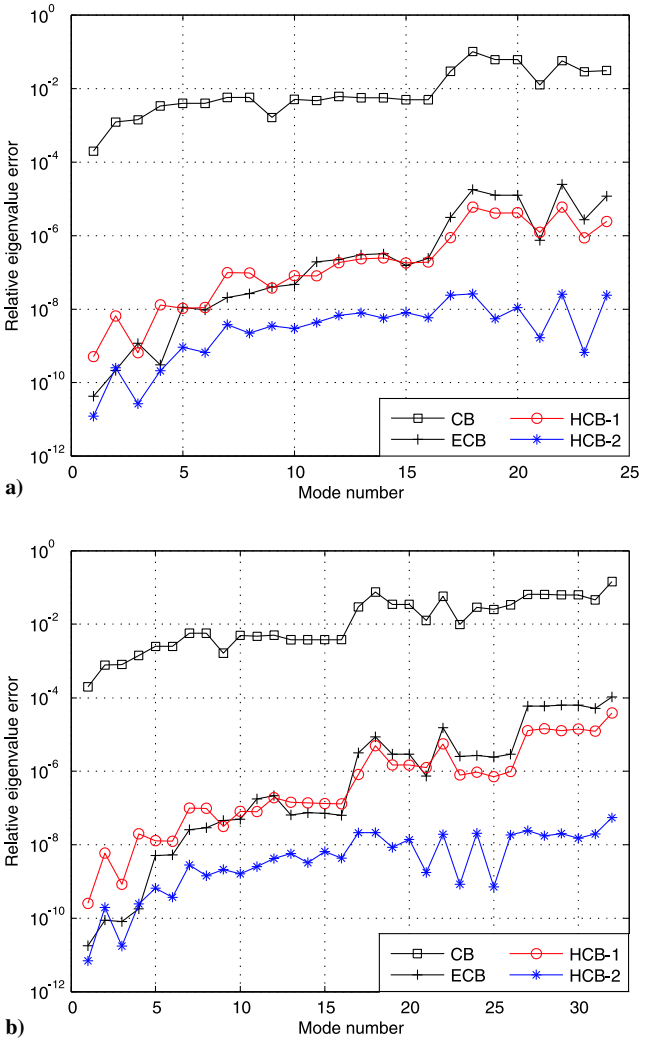

Fig. 8 Relative eigenvalue errors for the hyperboloid shell problem: a) $N_d = 24$, and b) $N_d = 32$.

B. Cylindrical Panel Problem

A cylindrical panel with free boundary is considered as shown in Fig. 5. The length L is 0.8 m, radius R is 0.5 m, and thickness is 0.005 m. Young's modulus E is 69 GPa, Poisson's ratio ν is 0.35, and density ρ is 2700 kg/m^3.

The cylindrical panel is modeled by a 16×16 distorted mesh of finite shell elements [32–35], in which each edge is discretized in the following ratio:

$$L_1 : L_2 : L_3 : \cdots : L_{16} = 16 : 15 : 14 : \cdots\cdots : 1 \tag{35}$$

The number of DOFs is 1445 ($N_g = 1445$). The FE model is partitioned into seven substructures ($N_s = 7$).

We consider two numerical cases with 20 and 40 dominant modes selected ($N_d = 20$ and $N_d = 40$). The number of modes selected in each substructure ($N_d^{(k)}$) is listed in Table 3. Figure 6 presents the relative eigenvalue errors obtained using the CB, ECB, HCB-1, and HCB-2 methods. The results consistently demonstrate the improved accuracy of the HCB methods.

C. Hyperboloid Shell Problem

We consider a hyperboloid shell structure with free boundary in Fig. 7. The height H is 4.0 m, and thickness is 0.05 m. Young's modulus E is 69 GPa, Poisson's ratio ν is 0.35, and density ρ is 2700 kg/m^3. The midsurface of this shell structure is described by

$$x^2 + y^2 = 2 + z^2; \qquad z \in [-2, 2] \tag{36}$$

The hyperboloid shell structure is modeled using a 40×20 mesh of the four-node MITC shell elements [32–35]. The number of DOFs

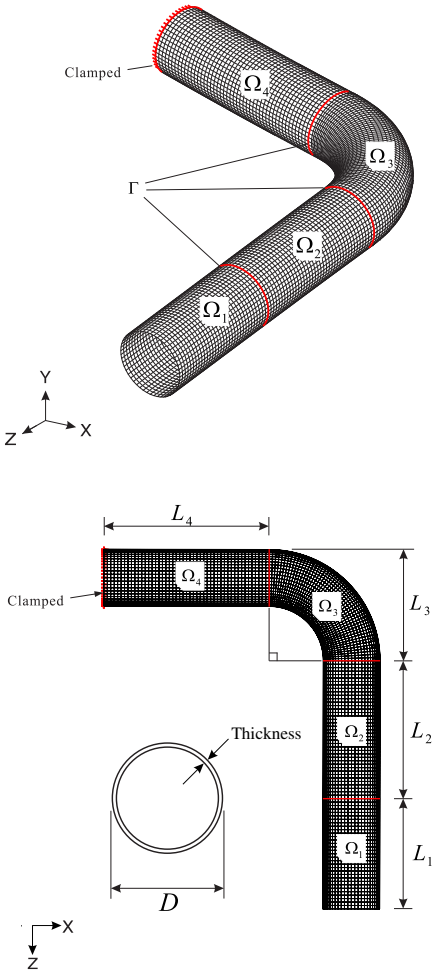

Fig. 9 Bent pipe problem (four substructures).

Table 5 Numbers of dominant modes selected for the bent pipe problem

Case	$N_d^{(1)}$	$N_d^{(2)}$	$N_d^{(3)}$	$N_d^{(4)}$	N_d	N_g
1	10	10	10	10	40	44,728
2	25	25	25	25	100	44,728

used is 4200 ($N_g = 4200$), and the FE model is partitioned into eight substructures ($N_s = 8$).

Two numerical cases are considered with 24 and 32 dominant modes selected ($N_d = 24$ and $N_d = 32$). The number of modes selected in each substructure ($N_d^{(k)}$) is listed in Table 4. Figure 8 presents the relative eigenvalue errors obtained using the CB, ECB, HCB-1, and HCB-2 methods. The results demonstrate the excellent performance of the HCB methods.

D. Bent Pipe Problem

We consider a bent pipe structure with clamped-free boundary in Fig. 9. The lengths L_1, L_2, L_3, and L_4 are 12.0, 15.0, 9.0, and 18.0 m, respectively, and the bent angle is 90 deg. Diameter D is 0.168 m, and thickness is 0.01 m. Young's modulus E is 204 GPa, Poisson's ratio ν is 0.35, and density ρ is 2700 kg/m^3. The bent pipe structure is modeled using the four-node MITC shell elements [32–35]. The number of DOFs used is 44,728 ($N_g = 44,728$), and the FE model is partitioned into four substructures ($N_s = 4$).

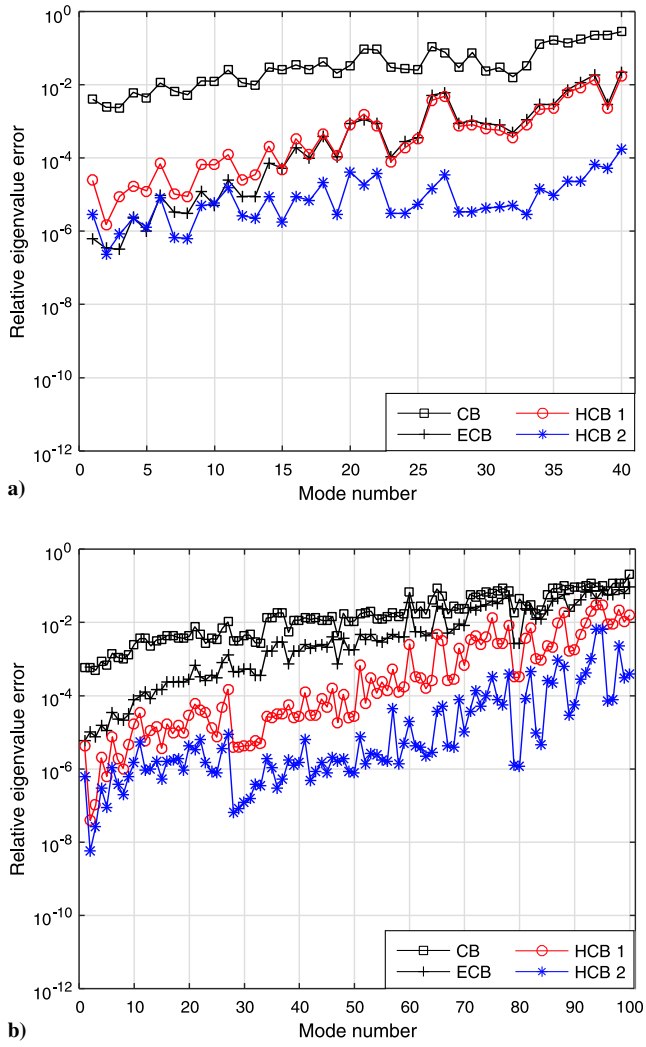

Fig. 10 Relative eigenvalue errors for the bent pipe problem: a) $N_d = 40$, and b) $N_d = 100$.

Two numerical cases are considered with 40 and 100 dominant modes selected ($N_d = 40$ and $N_d = 100$). The number of modes selected in each substructure ($N_d^{(k)}$) is listed in Table 5. Figure 10 presents the relative eigenvalue errors obtained using the CB, ECB, HCB-1, and HCB-2 methods. From the results, the improved accuracy of the HCB methods is well observed.

V. Computation Time

In this section, we compare the computation times required for the CB and HCB methods. An automobile wheel with free boundary is considered as shown in Fig. 11. The outer diameter is 0.482 m (19 in.), Young's modulus E is 210 GPa, Poisson's ratio ν is 0.3, and density ρ is 7850 kg/m^3. The automobile wheel problem is modeled using three-dimensional solid finite elements, and the finite element model is partitioned into four substructures ($N_s = 4$). The number of DOFs used is 54,930 ($N_g = 54,930$).

We establish an error criterion, namely that the relative eigenvalue errors up to the 100th mode are less than 10^{-4}, and we investigate the reduced models obtained by the three methods (CB, HCB-1, and HCB-2) until satisfying the given error criterion. Figure 12a presents the relative eigenvalue errors when the same size of reduced models is constructed. For the three methods, we select the same number of dominant modes, $N_d = 100$, as listed in Table 6. The HCB-2 method provides significantly better accuracy in the whole range of modes compared to others. Also, we can identify that the HCB-2 method is only satisfying the given error criterion.

In each model reduction method, the number of dominant modes selected is determined to satisfy the criterion; see Table 7. Figure 12b shows that all of the methods satisfy the criterion. Although the original CB method satisfies the criterion with 7000 dominant modes, the HCB-2 method requires only 100 dominant modes.

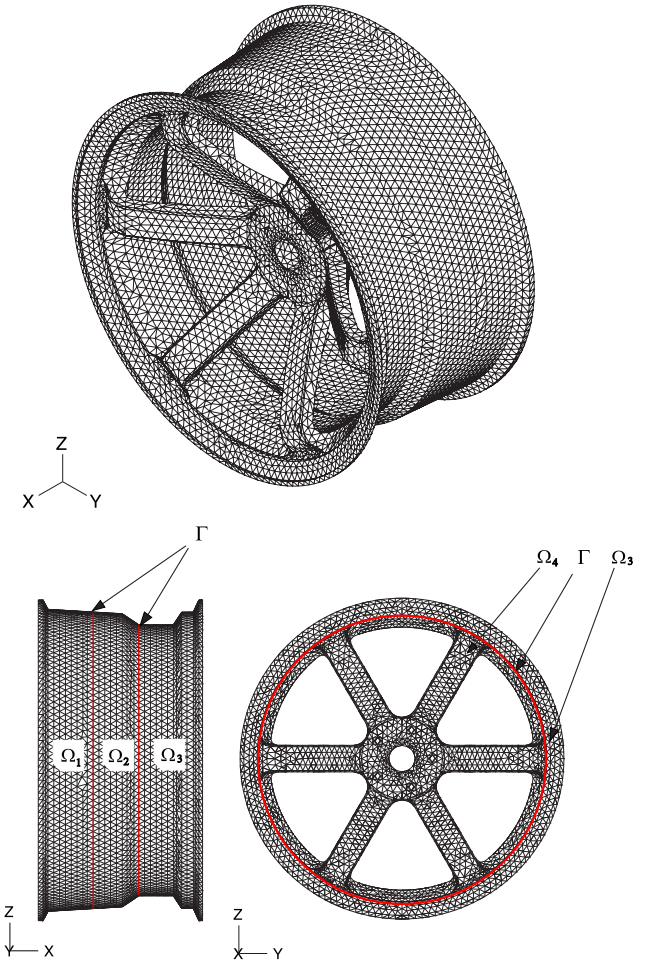

Fig. 11 Automobile wheel problem (four substructures).

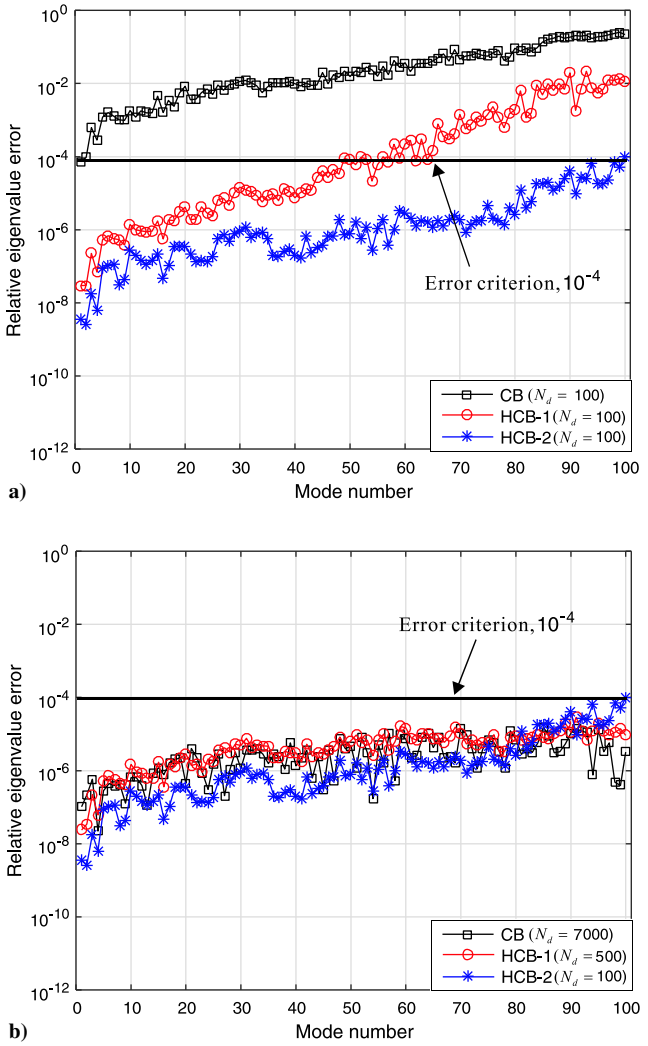

Fig. 12 Relative eigenvalue errors for the automobile wheel problem with the error criterion.

Table 8 presents the computation times required. The results show that the HCB-2 method produces the reduced model satisfying the criterion with less computation time than the CB method, even though using 70 times fewer modes.

In addition, we investigate the computation times for calculating 100 eigenpairs in the global and reduced models of the automobile wheel problem. Table 9 shows the computation times. The reduced model requires 3.41 s, whereas the global model requires 15.95 s. The results demonstrate the well-known advantage of reduced-order models from the computational point of view.

Table 6 Numbers of dominant modes selected for the automobile wheel problem in Fig. 12a

Method	$N_d^{(1)}$	$N_d^{(2)}$	$N_d^{(3)}$	$N_d^{(4)}$	N_d	N_g
CB	25	25	25	25	100	54,930
HCB-1	25	25	25	25	100	54,930
HCB-2	25	25	25	25	100	54,930

Table 7 Numbers of dominant modes selected for the automobile wheel problem in Fig. 12b

Method	$N_d^{(1)}$	$N_d^{(2)}$	$N_d^{(3)}$	$N_d^{(4)}$	N_d	N_g
CB	1500	1500	1500	1500	6000	54,930
HCB-1	125	125	125	125	500	54,930
HCB-2	25	25	25	25	100	54,930

Table 8 Specific computation times for the automobile wheel problem in Fig. 12b

Items	Methods CB (N_d = 7000)	HCB-1 (N_d = 500)	HCB-2 (N_d = 100)
Solving the substructural eigenvalue problems $\boldsymbol{K}_s^{(i)}\boldsymbol{\Phi}_s^{(i)} = \boldsymbol{\Lambda}_s^{(i)}\boldsymbol{M}_s^{(i)}\boldsymbol{\Phi}_s^{(i)}$	1014.07	16.03	3.40
Calculating the constraint mode matrix $\boldsymbol{\Psi}_c$	395.78	395.78	395.78
Calculating the residual mode matrix $\boldsymbol{\Theta}_n$[a]	—	— 205.41	744.61
Conducting the transformation procedure	918.76	698.41	778.37
Conducting the SEREP procedure[a]	—	— 97.53	169.73
Solving the reduced eigenvalue problem	21.51	2.78	3.41
Total	2350.12	1415.94	2095.30

[a]Items only required in the HCB methods.

Table 9 Computation times for calculating 100 eigenpairs for the wheel problem

Model	Computation time CPU time, s	Ratio, %
Global model	15.95	100.00
Reduced model (by the HCB-2 method)	3.41	21.38

VI. Conclusions

In this study, a new component mode synthesis (CMS) method was developed. The method is based on the well-known Craig–Bampton (CB) method. Because the higher-order effects of residual modes is considered in the formulation, it is named the higher-order Craig–Bampton (HCB) method. In the HCB method, the unknown coefficients in the residual flexibility are considered as additional generalized coordinates, which are eliminated in the final formulation.

Through numerical examples, the performance of the HCB method was demonstrated. The numerical results were compared with the original CB method (CB) and the enhanced CB method (ECB). We observed that the HCB method could construct the reduced-order models with significantly improved accuracy. The computational efficiency of the HCB method was also tested. In future works, it will be valuable to improve the computational efficiency of the HCB methods.

Acknowledgments

This research was supported by a grant (KCG-01-2015-01) through the Disaster and Safety Management Institute funded by Korea Coast Guard of Korean government.

References

[1] Craig, R. R., and Kurdila, A. J., *Fundamentals of Structural Dynamics*, Wiley, 2006, pp. 531–564.

[2] Bathe, K. J., *Finite element procedure*, Prentice–Hall, 2006, pp. 875–895.

[3] Hurty, W. C., "Dynamic Analysis of Structural Systems Using Component Modes," *AIAA Journal*, Vol. 3, No. 4, 1965, pp. 678–685. doi:10.2514/3.2947

[4] Craig, R. R., and Bampton, M. C. C., "Coupling of Substructures for Dynamic Analysis," *AIAA Journal*, Vol. 6, No. 7, 1968, pp. 1313–1319. doi:10.2514/3.4741

[5] Kammer, D. C., and Triller, M. J., "Selection of Component Modes for Craig–Bampton Substructure Representations," *AIAA Journal*, Vol. 118, No. 2, April 1996, pp. 264–270.

[6] Givoli, D., Barbone, P. E., and Patlashenko, I., "Which Are the Important Modes of a Subsystem?" *International Journal for Numerical Methods in Engineering*, Vol. 59, No. 12, March 2004, pp. 1657–1678. doi:10.1002/(ISSN)1097-0207

[7] Liao, B. S., Bai, Z., and Gao, W., "The Important Modes of Subsystems: A Moment-Matching Approach," *International Journal for Numerical Methods in Engineering*, Vol. 70, No. 13, June 2007, pp. 1581–1597. doi:10.1002/(ISSN)1097-0207

[8] Benfield, W. A., and Hruda, R. F., "Vibration Analysis of Structures by Component Mode Substitution," *AIAA Journal*, Vol. 9, No. 7, 1971, pp. 1255–1261. doi:10.2514/3.49936

[9] Rubin, S., "Improved Component-Mode Representation for Structural Dynamic Analysis," *AIAA Journal*, Vol. 13, No. 8, 1975, pp. 995–1006. doi:10.2514/3.60497

[10] Hintz, R. M., "Analytical Methods in Component Modal Synthesis," *AIAA Journal*, Vol. 13, No.8, 1975, pp. 1007–1016. doi:10.2514/3.60498

[11] Craig, R. R., and Hale, A. L., "Block-Krylov Component Mode Synthesis Method for Structural Model Reduction," *AIAA Journal*, Vol. 11, No. 6, 1988, pp. 562–570.

[12] Craig, R. R., "Substructure Method in Vibration," *Journal of Vibration and Acoustics*, Vol. 117, No. 8, 1995, pp. 207–213. doi:10.1115/1.2838665

[13] MacNeal, R. H., "Hybrid Method of Component Mode Synthesis," *Computers & Structures*, Vol. 1, No. 4, 1971, pp. 581–601. doi:10.1016/0045-7949(71)90031-9

[14] Bourquin, F., "Component Mode Synthesis and Eigenvalues of Second Order Operators: Discretization and Algorithm," *Mathematical Modelling and Numerical Analysis*, Vol. 26, No. 3, 1992, pp. 385–423. doi:10.1051/m2an/1992260303851

[15] Rixen, D. J., "A Dual Craig–Bampton Method for Dynamic Substructuring," *Journal of Computational and Applied Mathematics*, Vol. 168, Nos. 1–2, 2004, pp. 383–391. doi:10.1016/j.cam.2003.12.014

[16] Bennighof, J. K., and Lehoucq, R. B., "An Automated Multi-Level Substructuring Method for Eigenspace Computation in Linear Elastodynamics," *SIAM Journal on Scientific Computing*, Vol. 25, No. 6, 2004, pp. 2084–2106. doi:10.1137/S1064827502400650

[17] Park, K. C., and Park, Y. H., "Partitioned Component Mode Synthesis via a Flexibility Approach," *AIAA Journal*, Vol. 42, No. 6, 2004, pp. 1236–1245. doi:10.2514/1.10423

[18] Bathe, K. J., and Jian, D., "Component Mode Synthesis with Subspace Iterations for Controlled Accuracy of Frequency and Mode Shape Solutions," *Computers & Structures*, Vol. 139, July 2014, pp. 28–32. doi:10.1016/j.compstruc.2014.03.003

[19] Kim, J. G., and Lee, P. S., "An Enhanced Craig–Bampton Method," *International Journal for Numerical Methods in Engineering*, Vol. 103, No. 2, 2015, pp. 79–93. doi:10.1002/nme.v103.2

[20] Kim, J. G., Boo, S. H., and Lee, P. S., "An Enhanced AMLS Method and Its Performance," *Computer Methods in Applied Mechanics and Engineering*, Vol. 287, April 2015, pp. 90–111. doi:10.1016/j.cma.2015.01.004

[21] Baek, S. M., "Study on the Multi-Level Substructuring Scheme and System Condensation for the Large-Scaled Structural Dynamic Analysis," Ph.D. Dissertation, Mechanical and Aerospace Engineering Dept., Seoul National Univ., Seoul, Republic of Korea, 2012.

[22] Boo, S. H., Kim, J. G., and Lee, P. S., "A Simplified Error Estimator for the CB Method and Its Application to Error Control," *Computers & Structures*, Vol. 164, Feb. 2016, pp. 53–62. doi:10.1016/j.compstruc.2015.11.003

[23] Boo, S. H., Kim, J. G., and Lee, P. S., "Error Estimation Method for Automated Multi-Level Substructuring Method," *International Journal for Numerical Methods in Engineering*, Vol. 106, No. 11, 2016, pp. 927–950. doi:10.1002/nme.v106.11

[24] Boo, S. H., and Lee, P. S., "A Dynamic Condensation Method Using Algebraic Substructuring," *International Journal for Numerical Methods in Engineering*, Vol. 109, No. 12, 2017, pp. 1701–1720.

[25] Boo, S. H., and Lee, P. S., "An Iterative Algebraic Dynamic Condensation Method and Its Performance," *Computers & Structures*, Vol. 182, April 2017, pp. 419–429. doi:10.1016/j.compstruc.2016.12.011

[26] O'Callahan, J., "A Procedure for an Improved Reduced System (IRS) Model," *Proceedings of the 7th International Modal Analysis Conference*, Union College, Las Vegas, NV, 1989, pp. 17–21.

[27] O'Callahan, J., Avitabile, P., and Riemer, R., "System Equivalent Reduction Expansion Process (SEREP)," *Proceedings of the 7th International Modal Analysis Conference*, Union College, Las Vegas, NV, 1989, pp. 29–37.

[28] Stewart, G. W., *Matrix Algorithms, Volume 1, : Basic Decompositions*, Soc. for Industrial and Applied Mathematics, Philadelphia, 1998, pp. 55–56.

[29] Golub, G. H., and Van Loan, C. F., *Matrix Computations*, 3rd ed., JHU Press, 2012, pp. 52–54.

[30] Van der Sluis, A., "Stability of the Solutions of Linear Least Squares Problems," *Numerische Mathematik Journal*, Vol. 23, No. 3, 1974, pp. 241–254. doi:10.1007/BF01400307

[31] Hurty, W. C., "A Criterion for Selecting Realistic Natural Modes of a Structure," Jet Propulsion Lab., TM33-364, Pasadena, CA, 1967.

[32] Bathe, K. J., and Dvorkin, E. N., "A Formulation of General Shell Elements – The Use of Mixed Interpolation of Tensorial Components," *International Journal for Numerical Methods in Engineering*, Vol. 22, No. 3, 1986, pp. 697–722. doi:10.1002/(ISSN)1097-0207

[33] Lee, P. S., and Bathe, K. J., "Development of MITC Isotropic Triangular Shell Finite Elements," *Computers & Structures*, Vol. 82, Nos. 11–12, 2004, pp. 945–962. doi:10.1016/j.compstruc.2004.02.004

[34] Lee, Y., Lee, P. S., and Bathe, K. J., "The MITC3 + Shell Finite Element and Its Performance," *Computers & Structures*, Vol. 138, July 2014, pp. 12–23. doi:10.1016/j.compstruc.2014.02.005

[35] Lee, Y., Jeon, H. M., Lee, P. S., and Bathe, K. J., "The Modal Behavior of the MITC3 + Triangular Shell Element," *Computers & Structures*, Vol. 153, June 2015, pp. 148–164. doi:10.1016/j.compstruc.2015.02.033

[36] Allemang, R. J., and Brown, D. L., "A Correlation Coefficient for Modal Vector Analysis," *Proceedings of the 1st International Modal Analysis Conference*, Union College, Orlando, FL, 1982, pp. 110–116.

C. Bisagni
Associate Editor